This is the accepted manuscript made available via CHORUS. The article has been published as:

Effect of A mixing on elastic modulus, cleavage stress, and shear stress in the Ti_{3}(Si_{x}Al_{1−x})C_{2} MAX phase

Woongrak Son, Huili Gao, Thien Duong, Anjana Talapatra, Miladin Radovic, and Raymundo Arróyave

Phys. Rev. B **95**, 235131 — Published 16 June 2017

DOI: 10.1103/PhysRevB.95.235131

Effect of A-mixing on elastic modulus, cleavage stress, and shear stress in $Ti_3(Si_xAl_{1-x})C_2$ MAX Phase.

Woongrak Son[a], Huili Gao[a], Thien Duong[a], Anjana Talapatra[a], Miladin Radovic[a], Raymundo Arróyave[a,*]

[a] *Department of Materials Science and Engineering , Texas A&M University, College Station, TX 77843-3123, United States*

Abstract

Solid solution MAX phases offer the opportunity for further tuning of the thermo-mechanical and functional properties of MAX phases, increasing their envelope of performance. Previous experimental results show that the lattice parameters of $Ti_3(Si_xAl_{1-x})C_2$ decrease, while the Young's modulus increases with increased Si content in the lattice. In this work, we present a computational investigation of the structural, electronic, and mechanical properties of $Ti_3(Si_xAl_{1-x})C_2$ (x= 0, 0.25, 0.5, 0.75, and 1). The solid solutions were modeled using special quasirandom structures (SQS) and calculated using Density Functional Theory (DFT), which is implemented in the Vienna Ab initio Simulation Package (VASP). The SQS structures represent random mixing of Al and Si in the A sublattice of 312 MAX phase and their structural, electronic, and mechanical properties were calculated and compared with experiments. We study the cleavage and slip behavior of $Ti_3(Si_xAl_{1-x})C_2$ to investigate the deformation behavior in terms of cleavage and shear. It has been shown that the cleavage between M and A layers results in increasing cleavage stress in $Ti_3(Si_xAl_{1-x})C_2$ as a function of Si content in the lattice. In addition, the shear deformation of hexagonal close packed $Ti_3(Si_xAl_{1-x})C_2$ under $\langle 2\bar{1}\bar{1}0\rangle$ {0001} and $\langle 0\bar{1}10\rangle$ {0001} results in increasing unstable stacking fault energy (USFE) and ideal shear strength (ISS) in $Ti_3(Si_xAl_{1-x})C_2$ as the system becomes richer in Si.

Keywords: MAX phases, DFT, elastic property, cleavage, SFE.

---

1. INTRODUCTION

$M_{n+1}AX_n$, or in short MAX, phases are nanolayered, hexagonal compounds, wherein $M_{n+1}X_n$ layers are interleaved with A layers. In these crystal systems, M is typically an early transition metal, A is an A-group element and X is carbon or nitrogen. MAX phases share some chemical similarities to their MX binaries, as both are elastically very stiff with high thermal and electrical conductivities and high thermal and thermodynamic stability at elevated temperatures. However, unlike binary MX carbides and nitrides, MAX phases are relatively soft and readily machinable with good thermal shock resistance and tolerance to damage. The unique combination of strong M-X bonds with relatively weaker M-A bonds is responsible for this unique combination of properties that places MAX phases somewhat between typical metals and typical ceramic/refractory materials. The suite of properties that MAX phases offer make them attractive for applications in the automotive and aerospace industries, among others [1–3].

Among the close to 70 pure MAX phases synthesized and characterized to date, the Al-containing MAX phases such as Ti_2AlC and Ti_3AlC_2 are some of the most important and technologically interesting members of the family as they are considered to be promising materials for high-temperature applications. Al-containing MAX phases are known to have excellent oxidation properties due to the formation of a highly passivating, continuous, alumina layer when exposed to high temperature oxidizing environments [4–6]. Moreover, these MAX phases exhibit self-healing behavior as cracks exposed to oxidizing environments can heal due to the formation of stable alumina inter-crack films as Al migrates from the

---

[*] Corresponding address: 218 RDMD, Mail Stop 3123, Texas A&M University, College Station, TX 77843-3123, United States, Tel.: +1 979-845-5416, Fax: +1 979-845-3081

Email address: `rarroyave@tamu.edu` (Raymundo Arróyave)

Al layer in order to react with atmospheric oxygen in high temperature environments [7]. While many Al-containing MAX phases have excellent oxidation resistance, their overall strength is low compared to other MAX phases. In contrast, Ti_3SiC_2—one of the most well characterized MAX phases to date—has excellent mechanical properties compared to other MAX phases [8, 9]. Recently, the scientific community has started to explore the composition space in the MAX phases beyond the pure form, with the ultimate goal of tuning their properties through alloying. In the context of the present research, the combination of Si and Al in the A lattice in Ti-C 312 MAX phases can result in MAX phases that not only have good oxidation resistance and self-healing characteristics, but that also have high mechanical strength [10].

Previous experimental work has shown that $Ti_3(Si_xAl_{1-x})C_2$ solid solutions are not only similar to Ti_3SiC_2 in terms of their (good) mechanical properties, but are also similar to Ti_3AlC_2 due to the formation of a continuous alumina layer. Zhou et al. [11] synthesized a series of solid solutions of $Ti_3(Si_xAl_{1-x})C_2$, with x up to 0.25. In their work, they found that while the c lattice parameter decreased, the a lattice parameter remained almost invariant as a function of composition. Incorporation of Si into the A layer resulted in a marked increase in the Vickers hardness (26%), flexural strength (12%) and compressive strength (29%). More importantly, Zhou et al. found that additions to Si had no deleterious effects on the oxidation resistance of the compounds since a continuous Al_2O_3 layer still formed when exposed to oxidizing environments at 1100^{o}C. While these results are remarkable, they are limited to a relatively narrow compositional range. More recently, Gao et al. [10] fabricated $Ti_3(Al_{1-x}Si_x)C_2$ solid solutions over the entire composition range and found a significant hardening effect at x=0.5, while the structural and physical properties (a/c lattice parameters, Young's, bulk and shear moduli) followed Vegard's Law.

In the computational arena, Wang et al provided lattice parameters and bulk modulus of $Ti_3(Si_xAl_{1-x})C_2$ based on first principles calculation [12]. The calculations were limited to the x=0.75 composition, with the study focusing mostly on the mechanical and electronic properties of the compounds. Detailed analysis of the electronic structure led the authors to conclude that the bonding character of $Ti_3(Si_{0.75}Al_{0.25})C_2$ changes significantly, with the Ti-Si and Ti-Al bonds becoming less covalent than the corresponding bonds in the end members.

The available experimental and computational work on the $Ti_3(Si_xAl_{1-x})C_2$ provides evidence to support the stability of solid solutions in this system over the entire solubility range. To expand upon prior work, we present a investigation of the structural, electronic, and mechanical properties of $Ti_3(Si_xAl_{1-x})C_2$ within a Density Functional Theory (DFT) formalism [13], and covering the entire composition range.

In this work, we focus on the cleavage and slip behaviors of $Ti_3(Si_xAl_{1-x})C_2$ MAX solid solutions. These types of studies have not been carried extensively in the literature and it is hoped that insights derived from these theoretical calculations can be used to shed light into experimental observations showing a higher intrinsic hardness in Ti_3SiC_2 than in Ti_3AlC_2. To study cleavage behavior, we investigate cleavage energy and cleavage stress of $Ti_3(Si_xAl_{1-x})C_2$ (x = 0, 0.25, 0.5, 0.75, 1). The system does not contain any defect or grain boundary effects so that the predicted cleavage behavior corresponds to the intrinsic behavior of these systems that result from changes in the chemical bonding between the M and A layers as a result of changes in composition of the A-sublattice.

In order to study the slip behavior in these systems we investigate the generalized stacking fault energy (GSFE) surface of the pure MAX phases and an alloy corresponding to 50-50 mixing in the A-sublattice. The motivation for this portion of the work presented here is to further elucidate the influence of chemical mixing in the A-sublattice on the mechanical properties of MAX solid solutions. Specifically, we are interested in understanding the barriers for dislocation slip along the basal plane of MAX phases. MAX phases, which are layered hexagonal structures, have a limited number of slip systems [14] and therefore the formation of stacking faults and the energy required to nucleate dislocations are important to study their behavior. The calculation of the GSFE surface involves the quantification of the response to shearing of specific crystal planes along specific slip directions. One of the first instances in which the GSFE surface for MAX phases was calculated was the work by Gouriet et al [15]. In that case, the GSFE was calculated by sliding (0001) planes at different cutting levels (i.e. probing the shear strength of M-A and M-X layers, respectively). The work by Gouriet suggests that in their system under investigation—Ti_2AlN—plastic deformation was effectively governed by dislocation slip within the M-A layer rather than the M-X layer as expected by the much weaker chemical bonding between M-A species. Their calculations, however, were somewhat limited as they only considered relaxation along the z direction, keeping the x and y coordinates fixed. In this work, by contrast, we employ the method suggested by Jahnátek et al [16], in which the GSFE surface is calculated through uniform shearing deformation of a structure. As will be described below, we considered different constraints to the relaxation of ions subject to this shear deformation, and accounted for affine (alias) deformation modes in which all the atoms move (or not) along the deformed lattice vectors.

2. COMPUTATIONAL DETAILS

2.1. Density Functional Theory (DFT)

In this study, the calculations were carried out through Density Functional Theory (DFT) [17], with projected augmented wave (PAW) pseudopotentials [18, 19] as implemented in the Vienna Ab-initio Simulation Package (VASP) [20, 21]. Exchange correlation was accounted for within the Perdew-Burke-Ernzerhof (PBE) approximation [22] and the electronic configurations for titanium, aluminum, silicon and carbon where chosen to be $[\mathrm{Ar}]3d^3 4s^1$, $[\mathrm{Ne}]3s^2 3p^1$, $[\mathrm{Ne}]3s^2 3p^2$ and $[\mathrm{He}]2s^2 2p^2$, respectively. Relaxations were done with the Methfessel-Paxton smearing method [23], relaxing first the volume, the shape and then all the atoms.

2.2. Special Quasirandom Structures (SQS)

The fully disordered crystalline alloys have to be obtained to investigate the solid solution of MAX phases. For a given number of atoms per supercell, SQS is known as the best periodic supercell approximation to the fully disordered crystalline alloys, within a given coordination shell. In the current work, the SQS structures are generated using the ATAT [24] package. The SQS generation algorithm is based on Monte Carlo simulated annealing relaxation of candidate configurations, with the objective of matching the largest number of random correlation functions derived from occupancies of different sites within a given symmetrically unique cluster/figure:

$$\rho_\alpha(\sigma) = \langle \Gamma_{\alpha'}(\sigma) \rangle_\alpha \qquad (1)$$

where, the σ, $\sigma_i = 0, \ldots, M_{i-1}$, denotes chemical species that occupy site i, the α, $\alpha_i = \alpha_i = 0, \ldots, M_{i-1}$, considers particular correlation called cluster, and $\langle \Gamma_{\alpha'}(\sigma) \rangle$ is a cluster function, defined as

$$\langle \Gamma_{\alpha'}(\sigma) \rangle = \Pi \gamma_{\alpha_i, M_i}(\sigma_i). \qquad (2)$$

Details of the approach can be found in Walle et al [24]. In this work, the SQS were generated to study $Ti_3(Si_xAl_{1-x})C_2$ solid solutions where x corresponds to 0.25, 0.5 and 0.75.

2.3. Elastic properties

The stress-strain approach was used to estimate the elastic constants of the MAX alloys[25–27]. For a set of strains ($\varepsilon = \varepsilon_1, \varepsilon_2, \varepsilon_3, \varepsilon_4, \varepsilon_5$ and ε_6) imposed on a crystal structure, the deformed lattice vectors are expressed by the following matrix:

$$\bar{A} = A \begin{vmatrix} 1+\varepsilon_1 & \frac{\varepsilon_6}{2} & \frac{\varepsilon_5}{2} \\ \frac{\varepsilon_6}{2} & 1+\varepsilon_2 & \frac{\varepsilon_4}{2} \\ \frac{\varepsilon_5}{2} & \frac{\varepsilon_4}{2} & 1+\varepsilon_3 \end{vmatrix}.$$

For the deformed crystals, a set of stresses ($\sigma = \sigma_1, \sigma_2, \sigma_3, \sigma_4, \sigma_5$ and σ_6) is calculated using the DFT methods. The elastic constants were calculated using Hooke's law from n set of strains and the resulting stresses, according to:

$$\begin{vmatrix} C_{11} & \cdots & C_{16} \\ \vdots & & \vdots \\ C_{61} & \cdots & C_{66} \end{vmatrix} =$$

$$\begin{vmatrix} \varepsilon_{1,1} & \cdots & \varepsilon_{1,n} \\ \vdots & & \vdots \\ \varepsilon_{6,1} & \cdots & \varepsilon_{6,n} \end{vmatrix}^{-1} \begin{vmatrix} \sigma_{1,1} & \cdots & \sigma_{1,n} \\ \vdots & & \vdots \\ \sigma_{6,1} & \cdots & \sigma_{6,n} \end{vmatrix}$$

The mechanical stability of the structures can be elucidated from the dependence of the strain energy on lattice distortions:

$$E = E_0 + \frac{1}{2} V_0 \sum_{i,j=1}^{6} C_{ij} \varepsilon_i \varepsilon_j + O(\varepsilon^3) \qquad (3)$$

Specifically, mechanical stability is ensured when the elastic constant tensor is positive definite. For an hexagonal lattice, the static, mechanical stability criterion is satisfied by the following conditions:

$$C_{44} > 0, C_{11} > |C_{12}|,$$
$$(C_{11} + 2C_{12})C_{33} > 2C_{13}^2. \qquad (4)$$

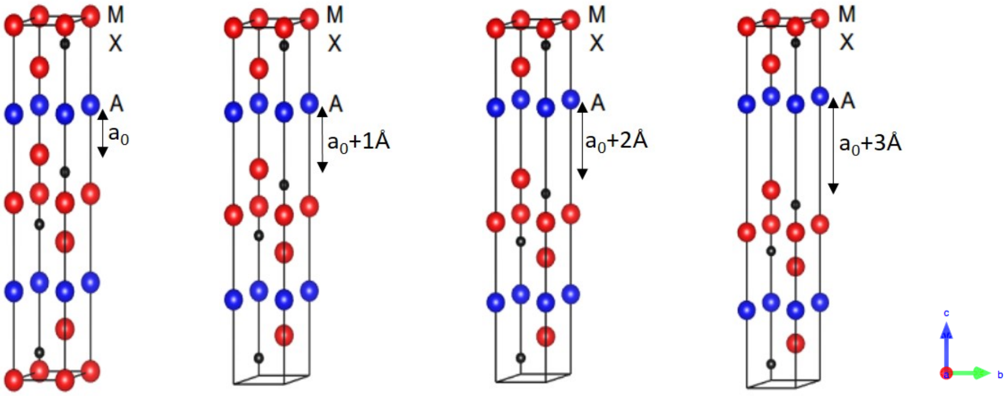

(a) z=0 (b) z=1 (c) z=2 (d) z=3

Figure 1: Cleavage between M and A layer under loading mode I. The cleavage distance z (Å) for (a), (b), (c) and (d) is 0, 1, 2 and 3, respectively.

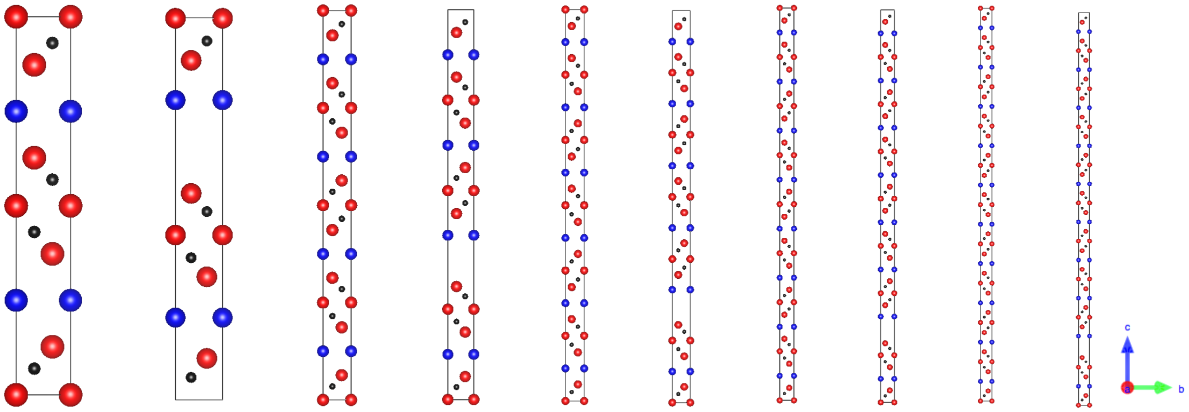

(a) (b) (c) (d) (e) (f) (g) (h) (i) (j)

Figure 2: Cleavage between M and A layer under loading mode I. The number of unit cells in the system before the cleavage of (a), (c), (e), (g), and (i) are 1, 2, 3, 4, and 5, respectively. The number of unit cell in the system after the cleavage of (b), (d), (f), (h), and (j) is 1, 2, 3, 4, and 5, respectively.

2.4. Cleavage energy

We implement a model for understanding cleavage behavior under loading mode I [28], which is shown in Fig. 1. In this mode, the tensile stress is loaded normal to the plane of the crack. In particular, we initiate a crack between the M and A layers since the M-A bond is relatively weak in MAX phases. The cleavage energy was then calculated using DFT, accounting for relaxation in which the position of the atoms are fixed in the x-y plane, while the z position of all the atoms are relaxed, except for the atoms on the cleavage surface, which were fixed in order to preserve the cleavage distance during relaxation. Note that this constrained relaxation scheme is required for the cleavage energy calculation but not for the GSFE calculations. The cleavage energy over a surface area, ΔE/A, and stress, σ, were obtained as follows:

$$\Delta E/A = E(z)/A - E(0)/A \tag{5}$$

,where z is the cleavage distance between M and A layers. The stress σ(z) is defined by the first derivative,

$$\sigma(z) = \left(\frac{dE}{dz}\right) \tag{6}$$

The critical stress, σ_c, is the maximum value of the cleavage stress, σ_c=max[$\sigma(z)$]. The critical stress is the tensile stress needed to cut the bonds between the given cleavage planes and is dependent on the direction since MAX phases are anisotropic materials [29]. The critical stress along the *c* direction is the minimum since the M-A bond is weakest bond in MAX phases. Zhou et al. [29] have reported that the M-X slabs are structurally stable, while the weak M-A bonds accommodate deformation at large strains. To clarify the influence of cleavage direction, we calculated the critical cleavage stress for Ti_3AlC_2 along the *a* and *c* directions. The calculated critical stress along the c direction is 22.63 GPa while the critical stress along the *a* direction is 249.28 GPa, which basically implies that no cleavage along a-direction is possible at all. To study cleavage behavior, we calculated cleavage energy and critical stress of $Ti_3(Si_xAl_{1-x})C_2$.

Under the cleavage process, we studied the elastic response of neighboring regions in the unit cell. In addition to the relaxation scheme described above, we also consider a so-called ideal brittle cleavage [28] scenario was considered in which the M-A layer is cleaved along the *c* direction, without allowing for any relaxation along the *c* direction. The cleavage energy and stress of the ideal brittle model are compared to those of the model considering relaxation to study the effect of elastic relaxation on cleavage energy, as the latter consists of two parts: the atomic de-cohesion energy and the strain energy released in the crystal on either side of the cleavage surface. For the relaxation model, two relaxation models are considered. First, the cleavage energy and stress are calculated under atomic relaxation along *c* direction. Second, the cleavage energy and stress are calculated under atomic relaxation along all directions. The atomic relation is considered on atoms not on the cleavage surfaces. In addition, the cleavage energy and stress of systems with 1,2,3,4, and 5 unit cells, as shown in Fig. 2, are calculated with all the systems containing one single cleavage surface. Each of the systems with different numbers of unit cells was cleaved along the *c* direction, with atoms not belonging to the cleavage surfaces relaxed along the *c* direction. The cleavage energy and stress are calculated by equation 5 , and 6 to study the effect of system size.

2.5. Stacking Fault Energy (SFE)

The most active slip system of hexagonal close packed structure is $\langle 2\bar{1}\bar{1}0\rangle\{0001\}$ slip system. The dislocation generated by $\langle 2\bar{1}\bar{1}0\rangle\{0001\}$ is described by the Burgers vector, b = 1/3 $\langle 2\bar{1}\bar{1}0\rangle\{0001\}$. This dislocation can be separated into two partial dislocations, which are $\langle 1\bar{1}00\rangle\{0001\}$ and $\langle 10\bar{1}0\rangle\{0001\}$, identical to $\langle 0\bar{1}10\rangle\{0001\}$. We present resultant energy curves under both of the $\langle 2\bar{1}\bar{1}0\rangle\{0001\}$ and $\langle 0\bar{1}10\rangle\{0001\}$ shear deformations.

The orthorhombic super cell, shown in Fig. 3, has been used to study shear deformation of hexagonal close packed (HCP) system for Ti_3AlC_2, $Ti_3(Al_{0.5}Si_{0.5})C_2$, and Ti_3SiC_2. The basal plane of the orthorhombic supercell is parallel to the basal plan of HCP system, which is {0001} plane. The *a*, *b*, and *c* lattice vectors are parallel to the $\langle 2\bar{1}\bar{1}0\rangle$, $\langle 0\bar{1}10\rangle$, and $\langle 0001\rangle$. Two different shear deformations, alias and affine, are applied to the orthorhombic super cell [16]. While affine shear deformation proportionally displaces all atoms along the shear direction, alias shear deformation, in contrast, displaces only the top layer along the shear direction. For both shear deformations, we considered two types of shearing, simple and pure shear. Simple shear does not relax shape, volume, and atomic coordinates of sheared system. On the other hand, pure shear fully relaxes shape, volume, and atomic coordinates while fixing the angle of shear, essentially relaxing all internal stresses except for the component(s) corresponding to the deformation process.

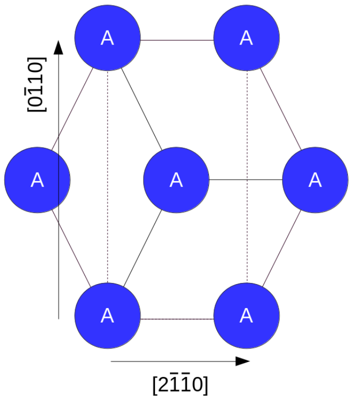

Figure 3: The orthorhombic super cell (dashed line) is used to investigate $\langle 2\bar{1}\bar{1}0\rangle$ {0001} and $\langle 0\bar{1}10\rangle$ {0001} shear deformation of hexagonal close packed (solid line) $Ti_3(Al_xSi_{1-x})C_2$ (x= 0, 0.5, and 1).

Currently, VASP does not allow one to carry on relaxations under arbitrary constraints and we thus used the external optimizer GADGET developed by Bucko et al to carry out full relaxation calculations by fixing the shear angle [30] and allowing all the other degrees of freedom to relax. The result of this constrained relaxation is the vanishing of all stress components of the stress tensor that do not explicitly correspond to the shear deformation applied on the structure and thus can be considered to be a more realistic deformation mechanism corresponding to dislocation slip along the basal plane [16].

3. RESULTS & DISCUSSION

3.1. Structural and Electronic Properties

The optimized structures of the $Ti_3(Si_xAl_{1-x})C_2$ are shown in Fig. 4, visualized using VESTA [31], in the form of hexagonal, nano-layered structures. The stability of $Ti_3(Si_xAl_{1-x})C_2$ is considered through the calculation of formation enthalpy $\Delta H(Ti_3(Si_xAl_{1-x})C_2)$ as given by

$$\Delta H(Ti_3(Si_xAl_{1-x})C_2) = E(Ti_3(Si_xAl_{1-x})C_2) \\ -nE(Ti) - nE(xSi) - nE((1-x)Al) - nE(C), \quad (7)$$

where E is the total energy per atom, n is a fraction of element in $Ti_3(Si_xAl_{1-x})C_2$ system, and x is a fraction of silicon in $Ti_3(Si_xAl_{1-x})C_2$ system. The calculated formation enthalpy of $Ti_3(Si_xAl_{1-x})C_2$ with x = 0, 0.25, 0.5, 0.75, 1 are -0.812, -0.826, -0.838, -0.849, -0.861, respectively in the unit of eV/atom.

The resultant lattice parameters of the $Ti_3(Si_xAl_{1-x})C_2$ are shown in Fig. 5(a), and compared to experimental results [10]. As it can be seen in Fig. 5(a), both of the calculated and experimental results show that the *c* lattice parameter decreases more than the *a* lattice parameter with increasing amount of Si. Fig. 5(b) shows that bond lengths of both M_1-X and M_2-X are constant, while that of M-A is decreasing with increasing amount of Si. The decreasing *c* lattice parameter be explained by stronger M-A bond with increasing amount of Si. To demonstrate this, analysis of ELF, charge density, and charge transfer were carried out and described in the following sections.

Fig. 6 corresponds to a 2-dimensional representation of the ELF for $Ti_3(Si_xAl_{1-x})C_2$ on the (100) plane [32]. The ELF represents the sum of squares of the wave function, which corresponds to the number of electrons. ELF is suitable for the observation of electrons in real space, which corresponds to chemical bonding of each atom, and it is scaled between zero and one. As can be seen from the figure, distributions of electrons between M-A and A-X bonds are getting higher and higher with increasing Si-content.

The strength of the bond is related to the charge density, and the (100) plane view of the charge density of $Ti_3(Si_xAl_{1-x})C_2$ is shown in Fig. 7. The charge density in Fig. 7 represents the absolute value of the charge, for instance, both of the positively charged and negatively charged elements show the positive value of charge density. High charge density of M and Si elements compare to the Al element indicates that both M-A and A-X bonds are stronger in the case of Si-contained MAX phases.

The charge transfer of each atom is calculated by the Bader code, and the number of valence electrons is shown in Table 1. In the $Ti_3(Si_xAl_{1-x})C_2$, the to-

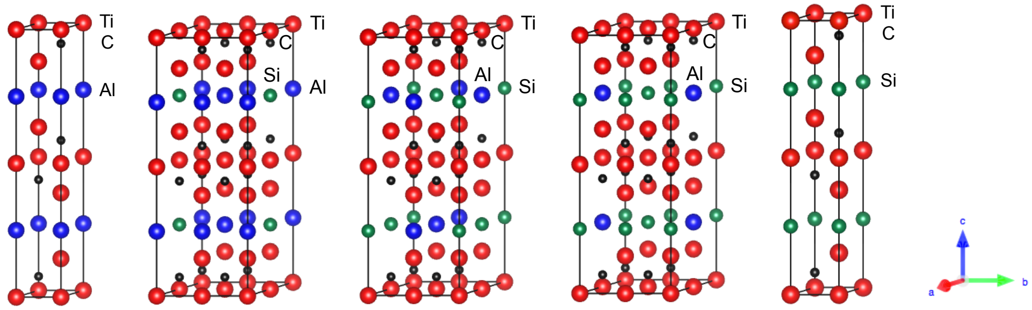

(a) x=0 (b) x=0.25 (c) x=0.5 (d) x=0.75 (e) x=1

Figure 4: Crystal structure of the $Ti_3Si_xAl_{1-x}C_2$ with (a) x=0, (b) x=0.25, (c) x=0.5, (d) x=0.75, and (e) x=1.

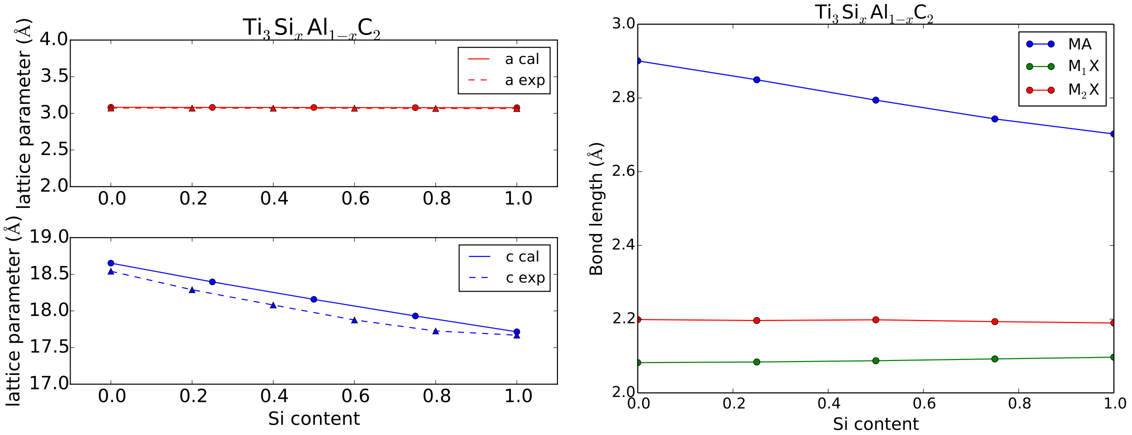

(a) Lattice parameters (b) Bond length

Figure 5: (a) The *a*- and *c*-lattice parameter as a function of Si composition, the solid lines represent the calculated data using DFT while the dash lines are the experimental data retrieved from XRD [10]. (b) Bond length of M-A, M_1-X, and M_2-X, where M_1 is a M element near the A element, and M_2 is a M element far from the A element.

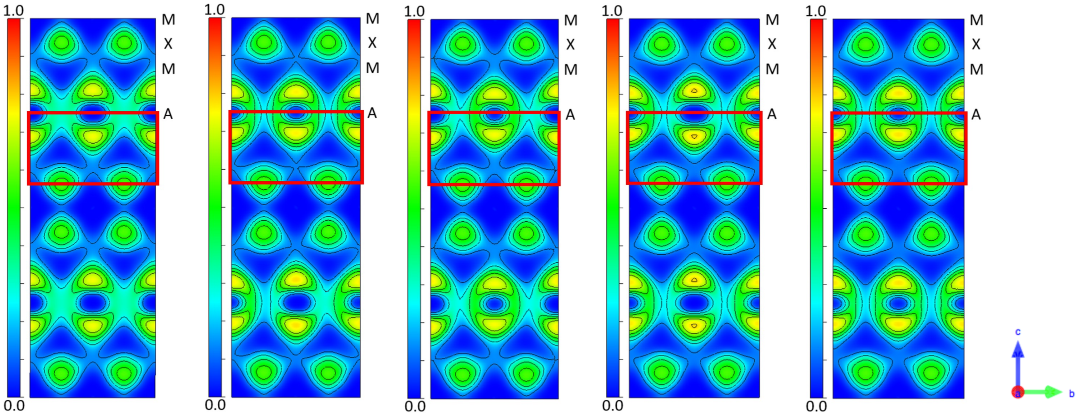

(a) x=0 (b) x=0.25 (c) x=0.5 (d) x=0.75 (e) x=1

Figure 6: (010) Plane view of Electron Localization Function (ELF) of the $Ti_3Si_xAl_{1-x}C_2$ with (a) x=0, (b) x=0.25, (c) x=0.5, (d) x=0.75, and (e) x=1.

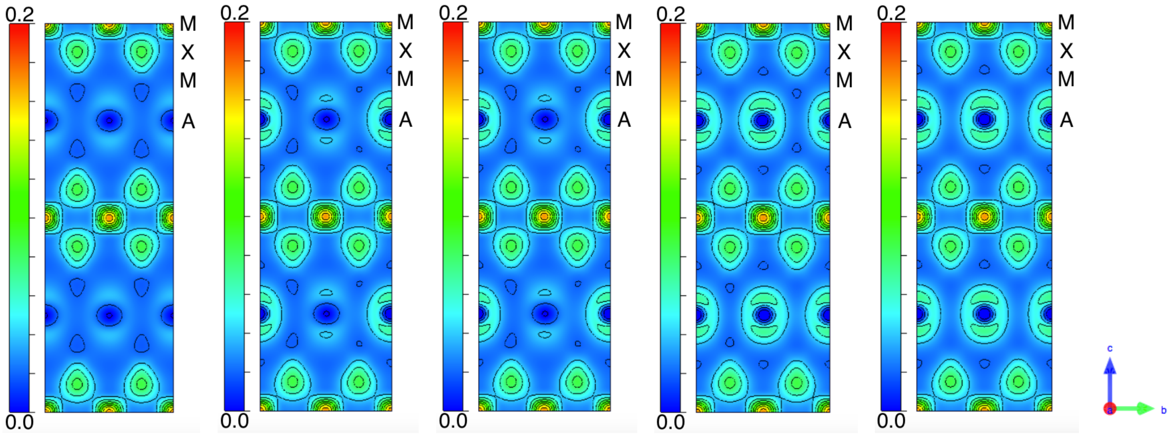

(a) x=0 (b) x=0.25 (c) x=0.5 (d) x=0.75 (e) x=1

Figure 7: (100) Plane view of charge density of the $Ti_3Si_xAl_{1-x}C_2$ with (a) x=0, (b) x=0.25, (c) x=0.5, (d) x=0.75, and (e) x=1.

Phase	Ti_3AlC_2	$Ti_3Si_{0.25}Al_{0.75}C_2$	$Ti_3Si_{0.5}Al_{0.5}C_2$	$Ti_3Si_{0.75}Al_{0.25}C_2$	Ti_3SiC_2
Ti (d3s1)	1.905 (-2.095)	1.896 (-2.104)	1.890 (-2.11)	1.885 (-2.115)	1.883 (-2.117)
Al (s2p1)	4.156 (+1.156)	4.093 (+1.093)	4.008 (+1.008)	3.826 (+0.826)	
Si (s2p2)		5.573 (+1.573)	5.539 (+1.539)	5.499 (+1.499)	5.378 (+1.378)
C (s2p2)	6.564 (+2.564)	6.550 (+2.550)	6.530 (+2.530)	6.507 (+2.507)	6.486 (+2.486)
Ti (total)	45.72	45.504	45.36	45.24	45.192
Al & Si (total)	33.248	35.704	38.188	40.646	43.024
C (total)	105.024	104.8	104.48	104.112	103.776

Table 1: The number of valence electrons is obtained by Bader analysis.

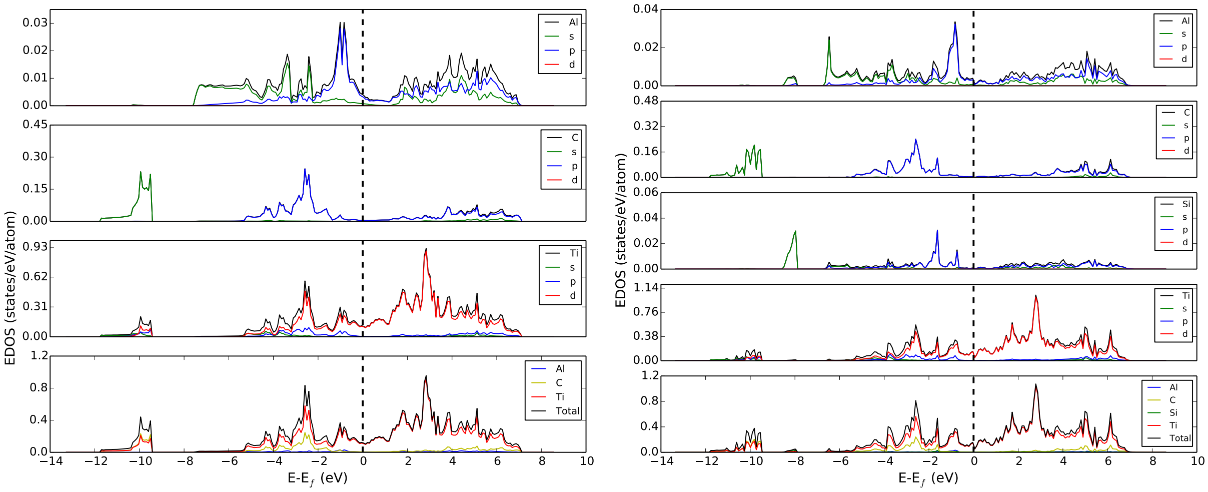

(a) Ti_3AlC_2 (b) $Ti_3(Si_{0.25}Al_{0.75})C_2$

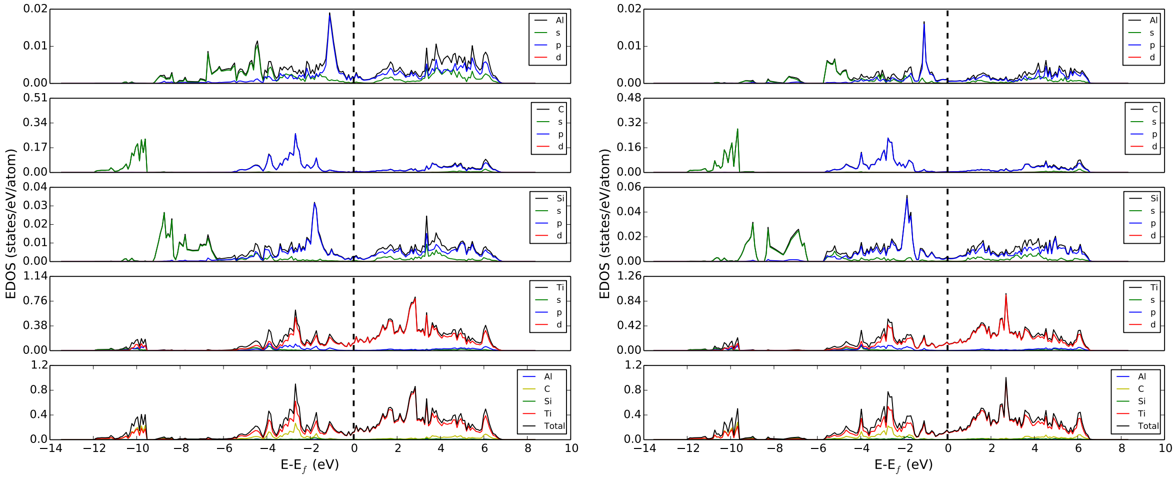

(c) $Ti_3(Si_{0.5}Al_{0.5})C_2$ (d) $Ti_3(Si_{0.75}Al_{0.25})C_2$

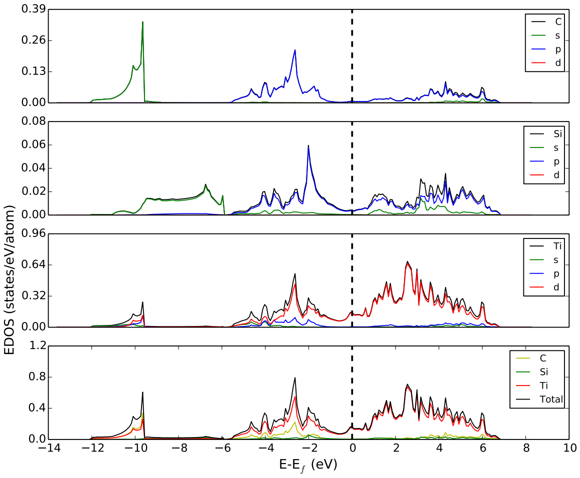

(e) Ti_3SiC_2

Figure 8: Calculated electronic density of states (EDOS) for (a) Ti_3AlC_2, (b) $Ti_3(Si_{0.25}Al_{0.75})C_2$, (c) $Ti_3(Si_{0.5}Al_{0.5})C_2$, (d) $Ti_3(Si_{0.75}Al_{0.25})C_2$, and (e) Ti_3SiC_2. The bottom panel indicates total and atom-projected DOS. The upper panels indicate site-projected DOS. The dashed line indicates the Fermi level.

tal charge density of Ti and C change from 45.72 to 45.192, and 105.024 to 103.776, respectively. Both Ti and C total charge density are almost constant. However, the total charge density of Al and Si changes from 33.248 to 43.024. The increasing charge density of Al and Si essentially affects the lattice parameter.

The total and atom-projected DOS for the $\mathrm{Ti_3(Si}_x\mathrm{Al}_{1-x})\mathrm{C_2}$ are shown in Fig. 8. The total DOS of $\mathrm{Ti_3(Si}_x\mathrm{Al}_{1-x})\mathrm{C_2}$ shows that titanium mostly contributes to the DOS at Fermi level, specifically d-electrons. The conductivity of $\mathrm{Ti_3(Si}_x\mathrm{Al}_{1-x})\mathrm{C_2}$ comes from the electronic density of states of titanium's d-electrons. The atom-projected DOS shows that the peaks around -2.5 eV correspond to hybridized p-C and d-Ti states, the peaks around -1.0 eV correspond to hybridized p-Al and d-Ti states, and the peaks around -2.0 eV correspond to p-Si and d-Ti states. The energy range of the hybridization shows that the Ti-X bond is stronger than the Ti-A bond. Within Ti-A bondings, the Ti-Si bond is stronger than the Ti-Al bond. This essentially implies stronger elastic properties of Si-contained MAX phases compared to those of $\mathrm{Ti_3AlC_2}$. The detailed investigation of such has been conducted and is presented below.

3.2. Elastic properties

Under the ground state condition, the elastic constants were calculated by the stress-strain approach based on DFT, then related to mechanical properties using Voigt's approximation. In particular, B, G, and E of hexagonal structure are expressed as follows [33]:

$$B_V = \frac{2(C_{11}+C_{12})+4C_{13}+C_{33}}{9}, \tag{8}$$

$$G_V = \frac{M+12C_{44}+12C_{66}}{30}, \tag{9}$$

$$M = C_{11}+C_{12}+2C_{33}-4C_{13}, \tag{10}$$

$$E = \frac{9BG}{3B+G}, \tag{11}$$

where B, G, and E are bulk, shear, and Young's modulus, respectively. The resultant elastic constants, bulk, shear, and Young's modulus are summarized in Table 2. Here, it can be seen that the B, G, and E are increasing with increasing amount of Si on the A site. This could be attributed to the charge density shown in Table 1. In particular, the substitution of Al with Si increases the total charge density of the A element atoms from 33.248 to 43.024. However, the total charge density of M and X element atoms does not change significantly, i.e. only from 45.72 to 45.192, and 105.024 to 103.776, respectively. The increased charge density makes the M-A bonds stronger, and thus harder to stretch. The Young's modulus, shown in Fig. 9, agrees well with the available experimental data, which also linearly increase with increasing amount of Si on the A site. Moreover, in the $\mathrm{Ti_3(Si}_x\mathrm{Al}_{1-x})\mathrm{C_2}$, C_{11} changes from 355.45 GPa to 370.47 GPa, and C_{33} changes from 292.89 GPa to 349.71 GPa. The large change of C_{33} could be related to the large change of c lattice parameter shown in Fig. 5.

3.3. Cleavage energy

As aforementioned, the focus of the current work is on the cleavage and slip behavior of $\mathrm{Ti_3(Si,Al)C_2}$ alloys. This is to shed some light onto the experimental observations regarding the increase in hardness in the case of Si-contained MAX phases. The knowledge about cleavage and slip is also found to be of interest developing constitutive models aimed at predicting the mechanical properties of MAX phases in the continuum limit as cleavage/slip energy as a function of displacement and separation can be used to build cohesive zone models that account for the highly anisotropic behavior in these materials.

Here, we present the results of our investigation of the cleavage energy in these MAX alloys. The results of the calculated cleavage energies are shown in Fig. 10(a). As can be seen from this figure, the cleavage energy sharply increases up to 1 $\mathring{A}$ of cleavage distance, and it is almost constant around the cleavage distance of 3 $\mathring{A}$. The cleavage stress, shown in Fig. 10(b), is derived from the cleavage energy, and the maximum cleavage stress appears around the cleavage distance of 0.9 $\mathring{A}$. The critical stress (maximum cleavage stress) of $\mathrm{Ti_3(Si}_x\mathrm{Al}_{1-x})\mathrm{C_2}$ increases with increasing amount of Si, and it is shown in Fig. 10(c). In Table 3, we compared the calculated critical stress values of $\mathrm{Ti_3AlC_2}$ and $\mathrm{Ti_3SiC_2}$ with nano-indentation experimental data (intrinsic hardness) and not the Vickers hardness. When a large force is applied, Vickers hardness measurement (macroscopic hardness) captures the effect of defect and grain boundary effects on the deformation, and it is thus not surprising that the Vickers hardness is underestimated when compared to the intrinsic hardness and calculated cleavage stress [34]. One must consider, however, that there might be a few defect and grain boundary effects on the intrinsic hardness measurement so that it is underestimated when compared to the calculated

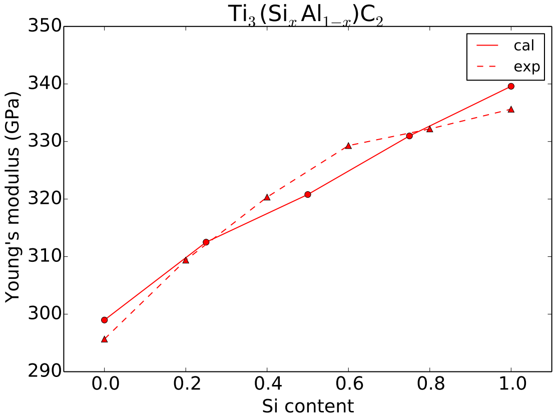

Figure 9: Comparison of Young's modulus obtained by DFT calculations (cal.) and RUS measurements (exp.) [10].

Phase	C_{11}	C_{33}	C_{44}	C_{12}	C_{13}	B	G	E
Ti_3AlC_2	355.45	292.89	119.03	84.63	76.03	163.02	125.17	298.98
$Ti_3Si_{0.25}Al_{0.75}C_2$	362.45	304.47	128.30	85.75	82.73	170.20	130.87	312.51
$Ti_3Si_{0.5}Al_{0.5}C_2$	365.02	317.32	136.93	90.32	90.99	176.88	133.91	320.79
$Ti_3Si_{0.75}Al_{0.25}C_2$	368.92	334.66	145.89	93.85	99.62	184.30	137.82	330.97
Ti_3SiC_2	370.47	349.71	155.43	97.22	112.11	192.61	140.78	339.60

Table 2: Elastic constants, bulk modulus (B), shear modulus (G), and Young's modulus (E).

		x=0	x=0.25	x=0.5	x=0.75	x=1
Critical stress (GPa)	calc	22.63	24.59	26.14	27.86	29.71
Intrinsic hardness (GPa)	exp	11.4 [34]				26 [35]

Table 3: Calculated maximum cleavage stress (critical stress) values of $Ti_3(Si_xAl_{1-x})C_2$, and experimentally reported intrinsic hardness of Ti_3AlC_2 and Ti_3SiC_2.

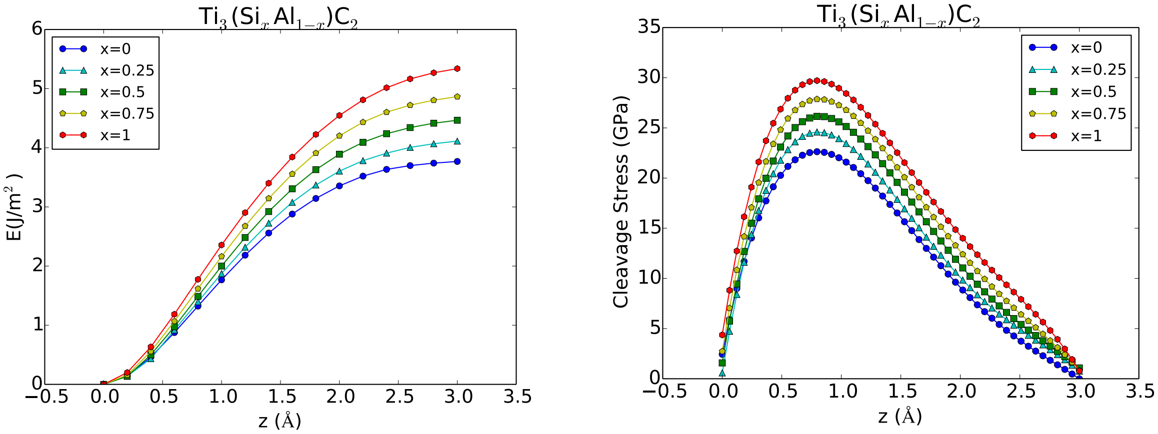

(a) Cleavage energy

(b) Cleavage stress

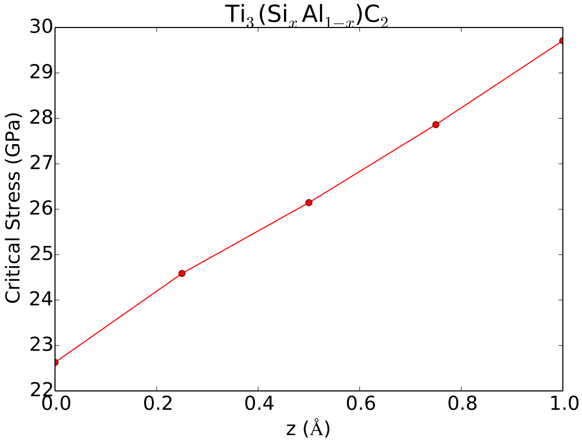

(c) Critical stress

Figure 10: a) Cleavage energy, b) cleavage stress, c) critical stress of the $Ti_3(Si_xAl_{1-x})C_2$.

cleavage stress. Also tension-shear coupling would lower the upper limit of the cleavage stress in an indentation experiment [36]. Our calculations do not include the effects of defects and grain boundaries, so the calculated cleavage energy and cleavage stress show purely the chemical effect, which is related to the bond strengths in the $Ti_3(Si_xAl_{1-x})C_2$ system.

To account for the effect of elastic relaxation upon cleavage, we studied the elastic response of neighboring regions in unit cell of Ti_3AlC_2 system. In Fig. 11(a) and 11(b), ideal brittle model shows the higher cleavage energy and stress than relaxation model along *c* direction as a function of separation. The critical stress of ideal brittle model and relaxation model along *c* direction are 23.02 GPa and 22.63 GPa, respectively. In Fig. 11(c) and 11(d), ideal brittle model shows the higher cleavage energy and stress than relaxation model along all directions as a function of separation. The critical stress of ideal brittle model and relaxation model along all directions are 23.02 GPa and 22.63 GPa, respectively. The cleavage energy of ideal brittle model is composed of the decohesion energy and strain energy in the system, while relaxation model minimizes the strain energy and the decohesion energy is dominant during the cleavage process. In addition, the two different relaxation models show equal cleavage energy and stress. This analysis shows that the strain energy contributions to the cleavage energy in these systems arises from atomic relaxations along the *c* direction. The differences in energy and stress, however, are rather small, and it can be safely assumed that relaxation effects upon cleavage are not significant.

To further elucidate the effect of system size on our cleavage calculations, we studied the cleavage behavior of Ti_3AlC_2 systems with 1, 2, 3, 4, and 5 unit cells, along the *c* direction. The calculated cleavage energy and stress of each system is shown in Fig. 12(a), and Fig. 12(b). Our results suggest that the cleavage energy of all systems is increasing sharply around 1 $\mathring{A}$, and converging at 3 $\mathring{A}$ of cleavage distance. The cleavage stress of systems is derived from the cleavage energy and shows the maximum value around 0.9 $\mathring{A}$ of cleavage distance. The critical stress of 1, 2, 3, 4, and 5 systems are 22.66, 22.60, 22.57, 22.54, and 22.52 GPa, respectively. These calculations suggest that the size of the system do not affect the results of the cleavage energy/stress calculations and thus one can use a single unit cell and obtain results that correspond to the intrinsic cleavage behavior in the large N limit.

3.4. Stacking Fault Energy (SFE)

Energy and shear stress curves under $\langle 2\bar{1}\bar{1}0\rangle\,\{0001\}$ and $\langle 0\bar{1}10\rangle\,\{0001\}$ shear deformations for Ti_3AlC_2, $Ti_3(Al_{0.5}Si_{0.5})C_2$, and Ti_3SiC_2 are presented in Fig. 13 and Fig. 14, respectively. The energy variation is presented as a function of fraction of the Burgers vector, f_b. The maximum energy corresponds to the unstable stacking fault energy (USFE), which can be related to the energy needed for the dislocation nucleation [37]. The minimum energy is the intrinsic stacking fault energy (ISFE). The maximum shear stress corresponds to the ideal shear stress (ISS), which is related to the stress necessary for the formation of stacking faults. The pure alias shear deformation is a more reliable description of dislocation generation mechanism, since displacement is generated at top layer, and relaxation leads to displacement from top to lower layers. The USFE under pure alias shear deformation for Ti_3AlC_2, $Ti_3(Al_{0.5}Si_{0.5})C_2$, and Ti_3SiC_2 are presented in Fig. 15 and Table 4. The USFE increases with increasing Si so that the Ti_3AlC_2 is more ductile than Ti_3SiC_2. This could be related to the anisotropy ratio shown in Table 4. The anisotropy ratio, $2C_{44}/(C_{11}\text{-}C_{12})$, quantifies how easy or difficult the shear deformation is. The low anisotropy ratio values in Table 4 suggest that Ti_3AlC_2 is more ductile than the Ti_3SiC_2.

Under $\langle 0\bar{1}10\rangle\,\{0001\}$ shear deformation, the USFE increases with increasing Si. Up to 30 % of shear deformation, all the deformation modes are identical except for simple alias shear. Beyond 30 % of shear deformation, the energy of simple affine shear is higher than that of pure affine and alias shear. Investigation of pure shear deformation is important since it allows all the atoms to be fully relaxed so that the system is more stable than that of simple shear deformation. The unit cell angles and atomic positions and lattice orientations at various stages of shear are presented in Fig. 16. It can be seen in Fig. 16 that α is changing with constant β and γ unit cell angels, and that the stacking fault has generated at 1.0 and 2.3 of f_b under pure alias shear deformation. The dashed line, presented in Fig. 16(b), represents the cell containing M and A elements, and the cell angle α' is plotted in Fig. 16(a) to compare to α. Under pure alias shear deformation α' is decreasing like α. However, α' sharply increases at 1.0 and 2.3 of f_b, and it represents the generation of stacking fault. The USFE essentially results from the generation of stacking fault and not due to a change in Ti_3AlC_2 cell shape.

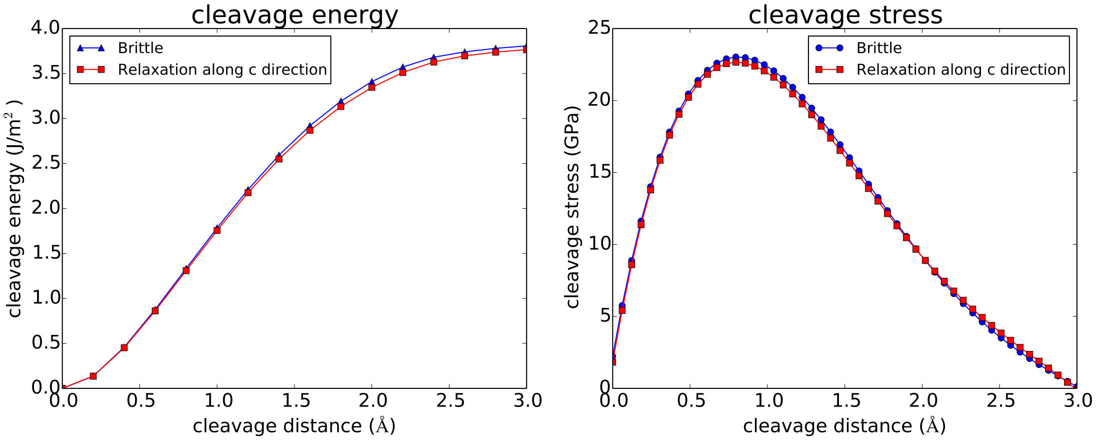

(a) Cleavage energy (b) Cleavage stress

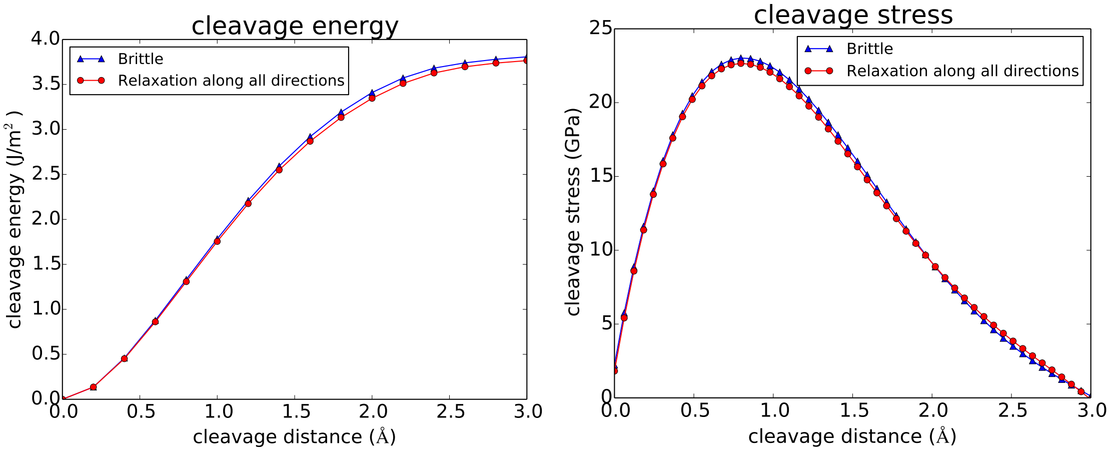

(c) Cleavage energy (d) Cleavage stress

Figure 11: a) and b) show the cleavage energy of ideal brittle model with relaxation model along *c* direction and all directions, respectively. c) and d) show the cleavage stress of ideal brittle model with relaxation model along *c* direction and all directions, respectively.

	Ti_3AlC_2	$Ti_3(Al_{0.5}Si_{0.5})C_2$	Ti_3SiC_2
USFE under $\langle 0\bar{1}10\rangle$ $\{0001\}$ pure alias shear deformation	1.34	1.45	1.71
USFE under $\langle 2\bar{1}\bar{1}0\rangle$ $\{0001\}$ pure alias shear deformation	0.56	0.79	1.02
$2C_{44}/(C_{11}\text{-}C_{12})$	0.879	0.997	1.138

Table 4: USFE in the unit of J/m^2 under $\langle 0\bar{1}10\rangle$ $\{0001\}$ and $\langle 2\bar{1}\bar{1}0\rangle$ $\{0001\}$ pure alias shear deformation, and the anisotropy ratio for Ti_3AlC_2, $Ti_3(Al_{0.5}Si_{0.5})C_2$, and Ti_3SiC_2.

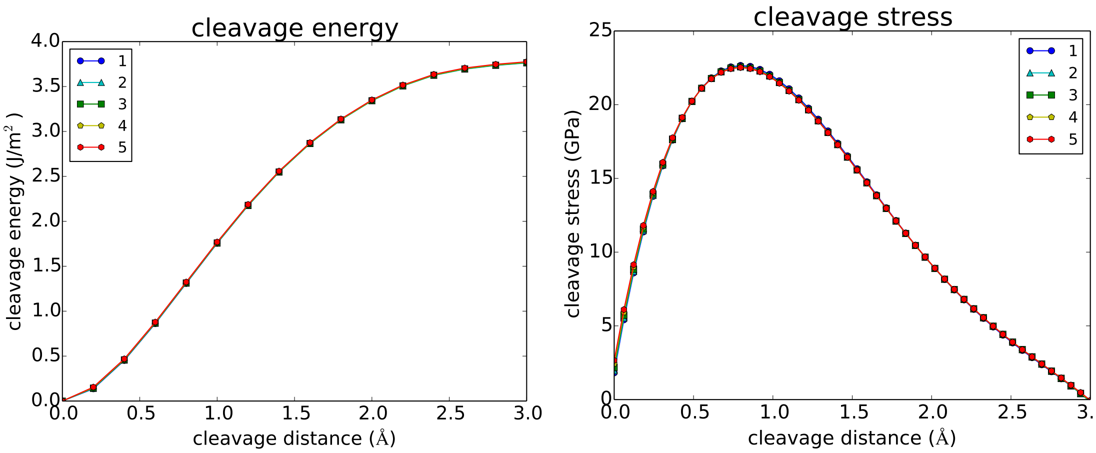

(a) Cleavage energy

(b) Cleavage stress

Figure 12: a) Cleavage energy, b) cleavage stress of 1, 2, 3, 4, and 5 unit cells in the Ti_3AlC_2 system with one cleavage surface.

Under $\langle 2\bar{1}\bar{1}0\rangle\,\{0001\}$ shear deformation, the USFE increases with increasing Si. Up to 20 % of shear deformation, all the deformation modes are identical except for simple alias shear. Beyond 20 % of shear deformation, the energy of simple affine shear is higher than that of pure affine and alias shear. As mentioned above, pure shear leads to more stable system than simple shear. The unit cell angles at various stages of shear are presented in Fig. 16. Unlike $\langle 0\bar{1}10\rangle\,\{0001\}$ shear deformation, α changes around 0.5 of f_b under $\langle 2\bar{1}\bar{1}0\rangle\,\{0001\}$ shear deformation, resulting in the USFE.

Both USFE under $\langle 2\bar{1}\bar{1}0\rangle\,\{0001\}$ and $\langle 0\bar{1}10\rangle\,\{0001\}$ shear deformation increase with increasing amount of Si. In addition, USFE under $\langle 2\bar{1}\bar{1}0\rangle\,\{0001\}$ shear deformation is lower than USFE under $\langle 0\bar{1}10\rangle\,\{0001\}$ shear deformation, thus $\langle 0\bar{1}10\rangle\,\{0001\}$ shear deformation will be preferable under the deformation behavior. To demonstrate this, analysis of ELF, charge density, and charge transfer were carried out. As shown in Fig. 17, distributions of electrons between M-A and A-X bonds are getting higher with increasing Si-content under both $\langle 2\bar{1}\bar{1}0\rangle\,\{0001\}$ and $\langle 0\bar{1}10\rangle\,\{0001\}$ shear deformations. This causes A elements to be charged more negatively with increasing Si-content. Fig. 18 shows the increased charge density of A element under both $\langle 2\bar{1}\bar{1}0\rangle\,\{0001\}$ and $\langle 0\bar{1}10\rangle\,\{0001\}$ shear deformations, which makes atomic bond between M-A layer stronger. The number of valence electrons per atom are shown in Table 5. The number of valence electrons of M and X elements are almost constant, while that of A element is increasing with increasing Si-content. This results in increasing USFE with increasing Si-content. In addition, the number of valence electrons of A element under $\langle 2\bar{1}\bar{1}0\rangle$ shear deformation is higher compared to that of A element under $\langle 0\bar{1}10\rangle$ shear deformation. Under $\langle 2\bar{1}\bar{1}0\rangle$ shear deformation, the strong atomic bond between M-A layer makes the system more stable than $\langle 0\bar{1}10\rangle$ shear deformation, thus $\langle 2\bar{1}\bar{1}0\rangle$ shear deformation will be preferable than $\langle 0\bar{1}10\rangle$ shear deformation.

4. CONCLUSION

In this work, we investigated the ground state structural, electronic, and mechanical properties of the $Ti_3(Si_xAl_{1-x})C_2$ using DFT. The lattice parameter decreases with increasing Si, and the Young's modulus increases with increasing amount of Si. This is due to the increasing charge density near the A element atom with increasing amount of Si. The cleavage stress is calculated from cleavage energy under the loading mode I. The cleavage stress is maximum around the 0.9 $\mathring{A}$ of the cleavage distance, and the maximum cleavage stress increases with increasing Si. The energy under affine and alias shear deformation with (pure) and without (simple) relaxation has been calculated. USFE increases with increasing Si, and dislocation is preferably generated under $\langle 2\bar{1}\bar{1}0\rangle$ shear deformation. We have investigated cleavage stress and shear stress to study how the system will be under the deformation. The critical stress (the maximum cleavage stress) of the

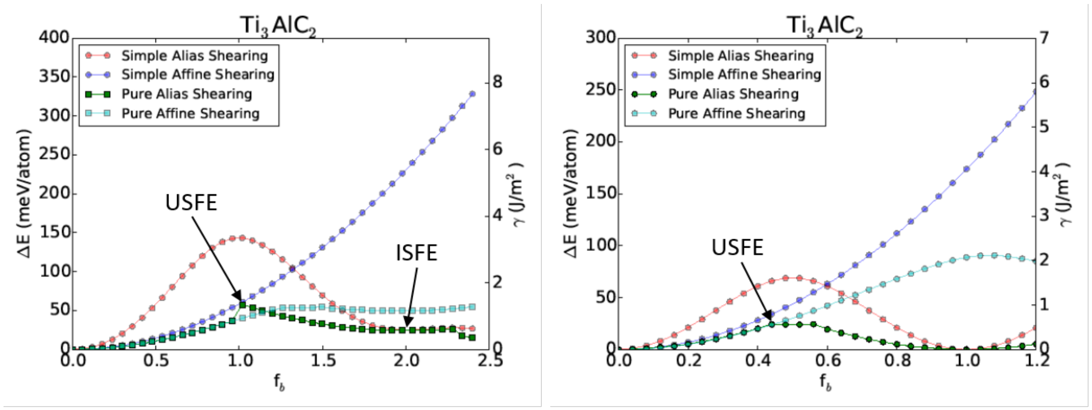

(a) Ti$_3$AlC$_2$

(b) Ti$_3$AlC$_2$

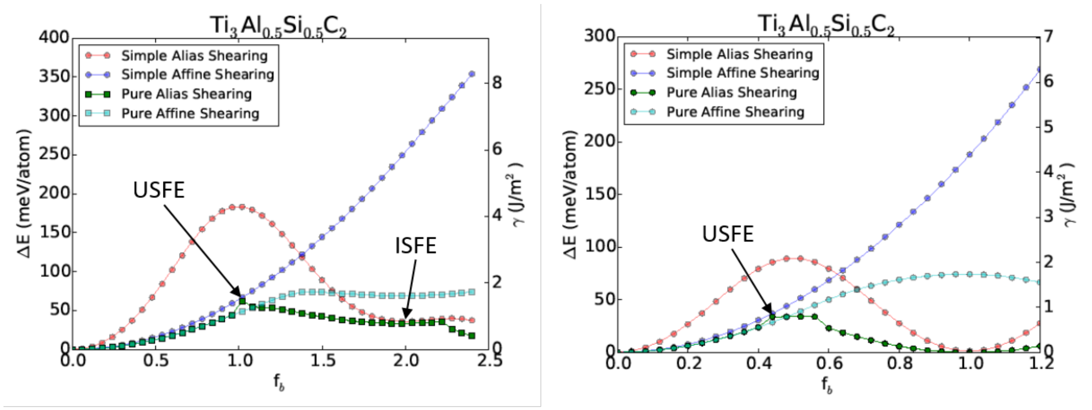

(c) Ti$_3$(Al$_{0.5}$Si$_{0.5}$)C$_2$

(d) Ti$_3$(Al$_{0.5}$Si$_{0.5}$)C$_2$

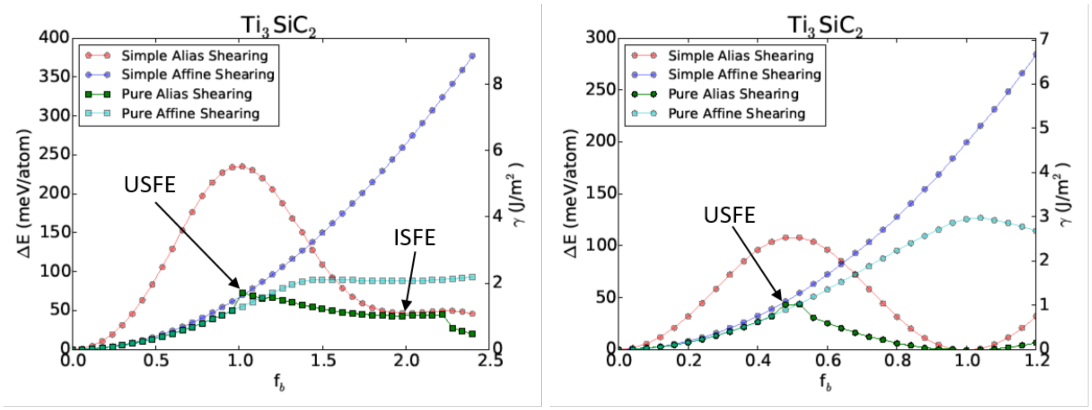

(e) Ti$_3$SiC$_2$

(f) Ti$_3$SiC$_2$

Figure 13: Energy as a function of fraction of Burgers vector, f$_b$. (a), (c), and (e) are under $\langle 0\bar{1}10\rangle$ $\{0001\}$ shear deformation for Ti$_3$AlC$_2$, Ti$_3$Al$_{0.5}$Si$_{0.5}$C$_2$, and Ti$_3$SiC$_2$, respectively. (b), (d), and (f) are under $\langle 2\bar{1}\bar{1}0\rangle$ $\{0001\}$ shear deformation for Ti$_3$AlC$_2$, Ti$_3$Al$_{0.5}$Si$_{0.5}$C$_2$, and Ti$_3$SiC$_2$, respectively.

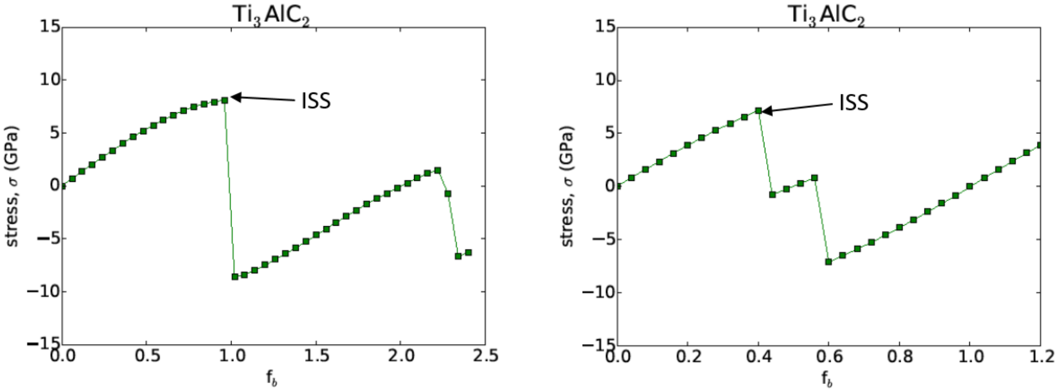

(a) Ti$_3$AlC$_2$

(b) Ti$_3$AlC$_2$

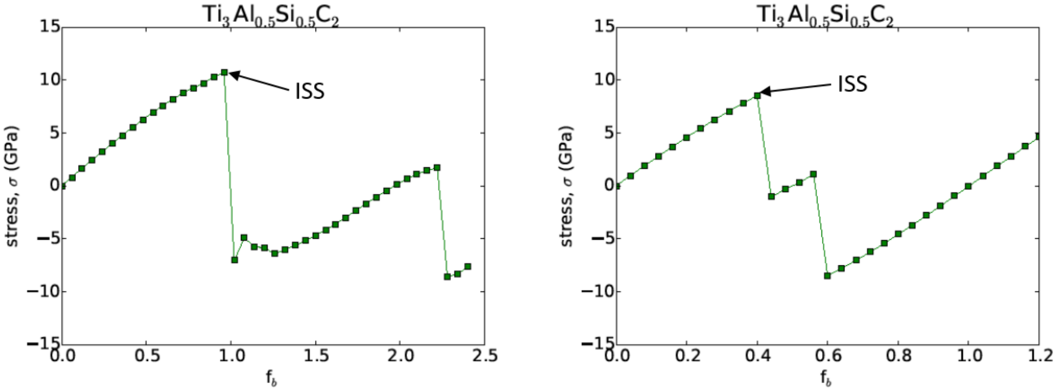

(c) Ti$_3$(Al$_{0.5}$Si$_{0.5}$)C$_2$

(d) Ti$_3$(Al$_{0.5}$Si$_{0.5}$)C$_2$

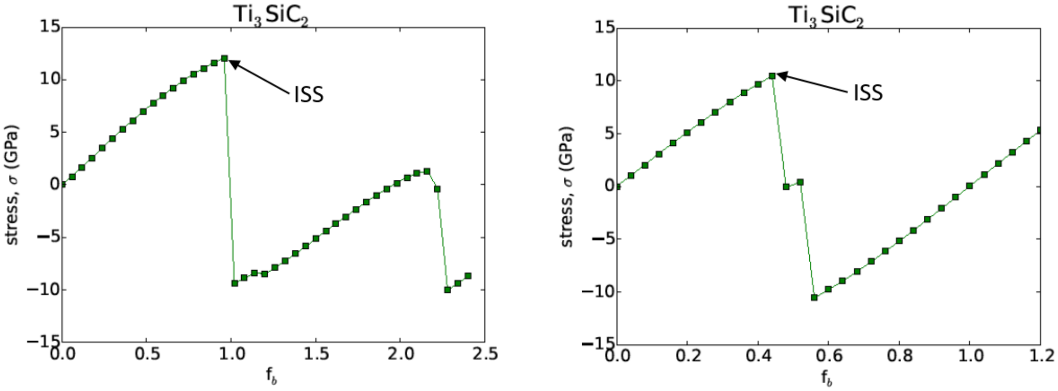

(e) Ti$_3$SiC$_2$

(f) Ti$_3$SiC$_2$

Figure 14: Shear stress as a function of fraction of Burgers vector, f$_b$. (a), (c), and (e) are under $\langle 0\bar{1}10\rangle$ $\{0001\}$ shear deformation for Ti$_3$AlC$_2$, Ti$_3$Al$_{0.5}$Si$_{0.5}$C$_2$, and Ti$_3$SiC$_2$, respectively. (b), (d), and (f) are under $\langle 2\bar{1}\bar{1}0\rangle$ $\{0001\}$ shear deformation for Ti$_3$AlC$_2$, Ti$_3$Al$_{0.5}$Si$_{0.5}$C$_2$, and Ti$_3$SiC$_2$, respectively.

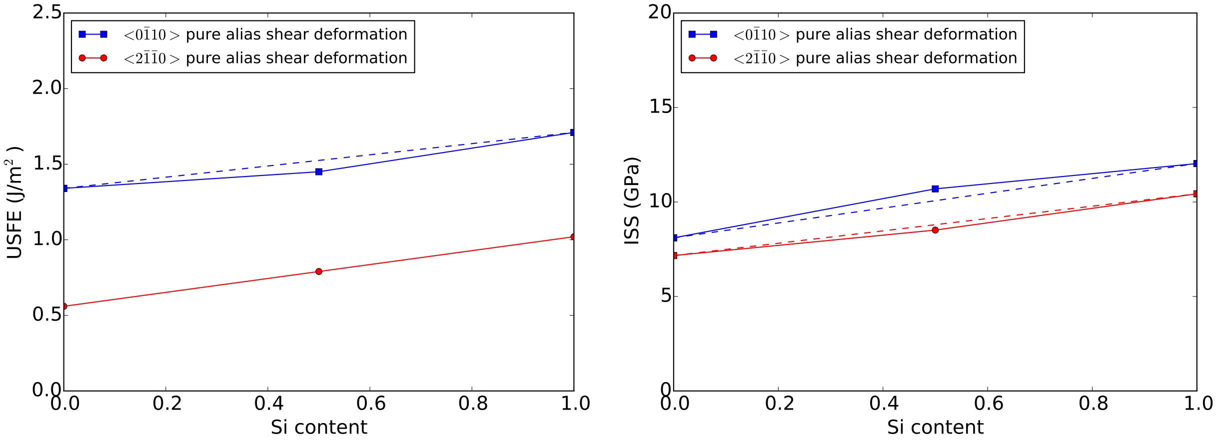

(a) Unstable Stacking Fault Energy (USFE).

(b) Ideal Shear Strength (ISS).

Figure 15: Variation of (a) USFE and (b) ISS under$\langle 0\bar{1}10\rangle$ and $\langle 2\bar{1}\bar{1}0\rangle$ pure alias shear deformation as a function of Si content.

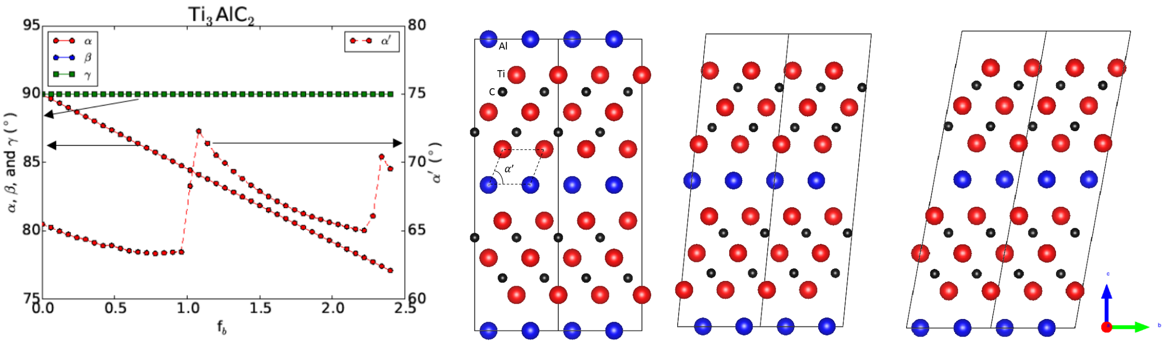

(a) $\langle 0\bar{1}10\rangle$ {0001} shear deformation

(b) f$_b$ = 0

(c) f$_b$ = 1.0

(d) f$_b$ = 2.0

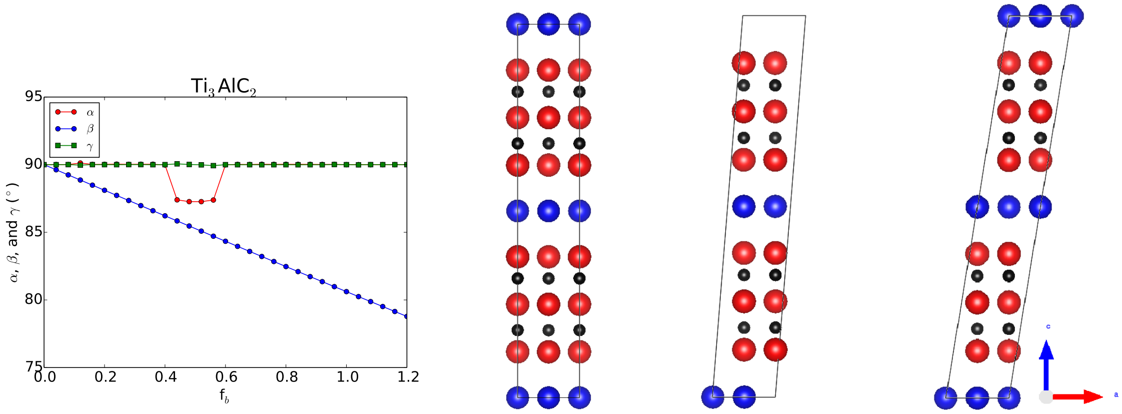

(e) $\langle 2\bar{1}\bar{1}0\rangle$ {0001} shear deformation

(f) f$_b$ = 0

(g) f$_b$ = 0.44

(h) f$_b$ = 1.0

Figure 16: (a) is unit cell angles of Ti_3AlC_2 system under $\langle 0\bar{1}10\rangle$ {0001} pure alias shear deformation. (b), (c), and (d) are Ti_3AlC_2 system under $\langle 0\bar{1}10\rangle$ {0001} pure alias shear deformation of f$_b$ = 0, 1.0, 2.0, respectively. (e) is unit cell angles of Ti_3AlC_2 system under $\langle 2\bar{1}\bar{1}0\rangle$ {0001} pure alias shear deformation. (f), (g), and (h) are Ti_3AlC_2 system under $\langle 2\bar{1}\bar{1}0\rangle$ {0001} pure alias shear deformation of f$_b$ = 0, 0.44, 1.0, respectively. Red, Blue and black atoms are Ti, Al, and C, respectively

Phase	Ti_3AlC_2	$Ti_3(Si_{0.5}Al_{0.5})C_2$	Ti_3SiC_2
$\langle 2\bar{1}\bar{1}0\rangle$ pure alias shear deformation			
Ti	1.91	1.90	1.89
Al & Si	4.11	4.72	5.33
C	6.58	6.55	6.51
$\langle 0\bar{1}10\rangle$ pure alias shear deformation			
Ti	1.92	1.90	1.89
Al & Si	4.07	4.68	5.27
C	6.59	6.56	6.53

Table 5: The number of valence electrons per atom at the level of USFE under $\langle 2\bar{1}\bar{1}0\rangle$ {0001} and $\langle 0\bar{1}10\rangle$ {0001} pure alias shear deformations.

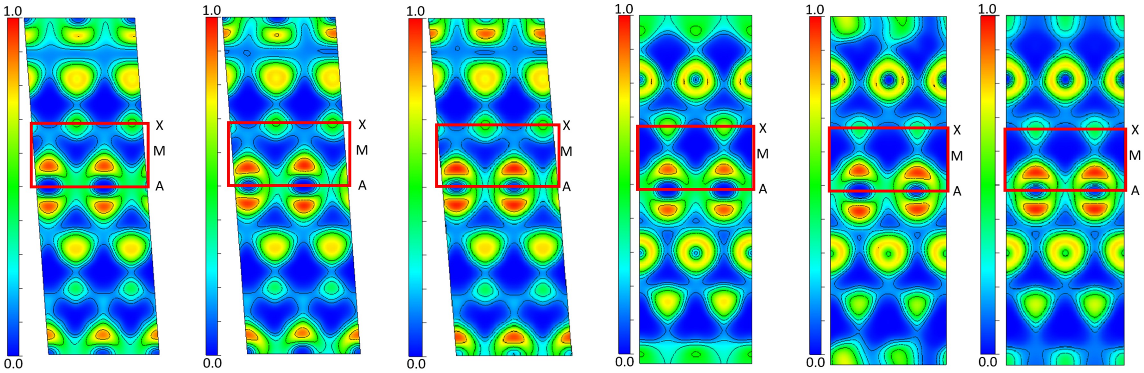

(a) x=0 (b) x=0.5 (c) x=1 (d) x=0 (e) x=0.5 (f) x=1

Figure 17: (010) Plane view of Electron Localization Function (ELF) under $\langle 2\bar{1}\bar{1}0\rangle$ {0001} pure alias shear deformation of $Ti_3(Si_xAl_{1x})C_2$ with (a) x=0, (b) x=0.5, (c) x=1, and $\langle 0\bar{1}10\rangle$ {0001} pure alias shear deformation with (d) x=0, (e) x=0.5, (f) x=1 at the level of USFE.

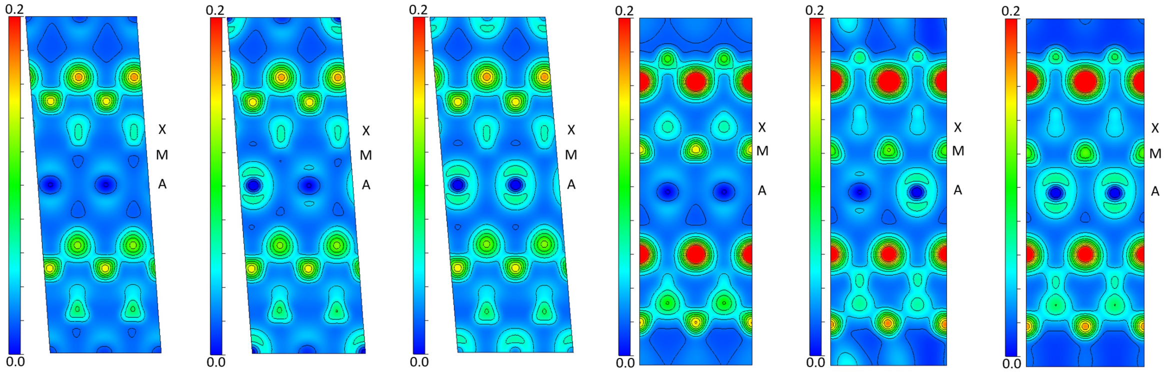

(a) x=0 (b) x=0.5 (c) x=1 (d) x=0 (e) x=0.5 (f) x=1

Figure 18: (010) Plane view of Charge density under $\langle 2\bar{1}\bar{1}0\rangle$ {0001} pure alias shear deformation of $Ti_3(Si_xAl_{1x})C_2$ with (a) x=0, (b) x=0.5, (c) x=1, and $\langle 0\bar{1}10\rangle$ {0001} pure alias shear deformation with (d) x=0, (e) x=0.5, (f) x=1 at the level of USFE.

$Ti_3(Si_xAl_{1-x})C_2$ is between 22.63 GPa and 29.71 GPa. The ideal shear stress (the maximum shear stress) of the $Ti_3(Si_xAl_{1-x})C_2$ under $\langle 2\bar{1}\bar{1}0\rangle$ shear deformation is between 7.16 GPa and 10.43 GPa, and under $\langle 0\bar{1}10\rangle$ is between 8.10 GPa and 12.03 GPa. The cleavage and shear analysis show that $\langle 2\bar{1}\bar{1}0\rangle$ shear deformation will be preferable under deformation.

5. ACKNOWLEDGMENTS

This work was funded through NSF Grand No. DMR-1410983. RA and AT acknowledge partial support from Grant AFOSR-FA9550-16-1-0180 (Program Manager: Ali Sayir). First-principles calculations were carried out in the Texas A&M Supercomputing Facility at Texas A&M University, and the Stampede Cluster at the Texas Advanced computing Center at University of Texas, Austin.

6. REFERENCES

[1] M. W. Barsoum, The m n+ 1 ax n phases: a new class of solids: thermodynamically stable nanolaminates, Progress in Solid State Chemistry 28 (1) (2000) 201–281.

[2] M. W. Barsoum, M. Radovic, Elastic and mechanical properties of the max phases, Annual review of materials research 41 (2011) 195–227.

[3] M. Radovic, M. W. Barsoum, Max phases: Bridging the gap between metals and ceramics, American Ceramics Society Bulletin 92 (3) (2013) 20–27.

[4] M. Sundberg, G. Malmqvist, A. Magnusson, T. El-Raghy, Alumina forming high temperature silicides and carbides, Ceramics International 30 (7) (2004) 1899–1904.

[5] X. Wang, Y. Zhou, High-temperature oxidation behavior of ti2alc in air, Oxidation of metals 59 (3-4) (2003) 303–320.

[6] G. Song, Y. Pei, W. Sloof, S. Li, J. T. M. De Hosson, S. Van der Zwaag, Oxidation-induced crack healing in ti 3 alc 2 ceramics, Scripta Materialia 58 (1) (2008) 13–16.

[7] H. Yang, Y. Pei, J. Rao, J. T. M. De Hosson, Self-healing performance of ti 2 alc ceramic, Journal of Materials Chemistry 22 (17) (2012) 8304–8313.

[8] M. Radovic, M. Barsoum, A. Ganguly, T. Zhen, P. Finkel, S. Kalidindi, E. Lara-Curzio, On the elastic properties and mechanical damping of ti 3 sic 2, ti 3 gec 2, ti 3 si 0.5 al 0.5 c 2 and ti 2 alc in the 300–1573k temperature range, Acta materialia 54 (10) (2006) 2757–2767.

[9] P. Finkel, M. Barsoum, T. El-Raghy, Low temperature dependencies of the elastic properties of ti 4 aln 3, ti 3 al 1.1 c 1.8, and ti 3 sic 2, Journal of Applied physics 87 (4) (2000) 1701–1703.

[10] H. Gao, R. Benitez, W. Son, R. Arroyave, M. Radovic, Structural, physical and mechanical properties of ti3(al1-xsix)c2 solid solution with x=0-1, Materials Science & Engineering A.

[11] Y. Zhou, J. Chen, J. Wang, Strengthening of ti 3 alc 2 by incorporation of si to form ti 3 al 1-x si x c 2 solid solutions, Acta materialia 54 (5) (2006) 1317–1322.

[12] J. Wang, Y. Zhou, First-principles study of equilibrium properties and electronic structure of ti3si0. 75al0. 25c2 solid solution, Journal of Physics: Condensed Matter 15 (35) (2003) 5959.

[13] N. Harrison, An introduction to density functional theory, NATO SCIENCE SERIES SUB SERIES III COMPUTER AND SYSTEMS SCIENCES 187 (2003) 45–70.

[14] M. Barsoum, T. Zhen, S. Kalidindi, M. Radovic, A. Murugaiah, Fully reversible, dislocation-based compressive deformation of ti3sic2 to 1 gpa, Nature Materials 2 (2) (2003) 107–111.

[15] K. Gouriet, P. Carrez, P. Cordier, A. Guitton, A. Joulain, L. Thilly, C. Tromas, Dislocation modelling in ti2aln max phase based on the peierls–nabarro model, Philosophical Magazine 95 (23) (2015) 2539–2552.

[16] M. Jahnátek, J. Hafner, M. Krajčí, Shear deformation, ideal strength, and stacking fault formation of fcc metals: A density-functional study of al and cu, Physical Review B 79 (22) (2009) 224103.

[17] W. Kohn, L. J. Sham, Self-consistent equations including exchange and correlation effects, Physical Review 140 (4A) (1965) A1133.

[18] J. P. Perdew, K. Burke, Y. Wang, Generalized gradient approximation for the exchange-correlation hole of a many-electron system, Physical Review B 54 (23) (1996) 16533.

[19] P. E. Blöchl, Projector augmented-wave method, Physical Review B 50 (24) (1994) 17953.

[20] G. Kresse, J. Furthmüller, Efficient iterative schemes for *ab initio* total-energy calculations using a plane-wave basis set, Phys. Rev. B 54 (1996) 11169–11186. doi:10.1103/PhysRevB.54.11169.

[21] G. Kresse, J. Furthmller, Efficiency of ab-initio total energy calculations for metals and semiconductors using a plane-wave basis set, Computational Materials Science 6 (1) (1996) 15 – 50. doi:http://dx.doi.org/10.1016/0927-0256(96)00008-0.

[22] M. Ernzerhof, G. E. Scuseria, Assessment of the perdew–burke–ernzerhof exchange-correlation functional, The Journal of chemical physics 110 (11) (1999) 5029–5036.

[23] M. Methfessel, A. T. Paxton, High-precision sampling for brillouin-zone integration in metals, Phys. Rev. B 40 (1989) 3616–3621. doi:10.1103/PhysRevB.40.3616.

[24] A. Van de Walle, P. Tiwary, M. De Jong, D. Olmsted, M. Asta, A. Dick, D. Shin, Y. Wang, L.-Q. Chen, Z.-K. Liu, Efficient stochastic generation of special quasirandom structures, Calphad 42 (2013) 13–18.

[25] S. Ganeshan, S. Shang, Y. Wang, Z.-K. Liu, Effect of alloying elements on the elastic properties of mg from first-principles calculations, Acta Materialia 57 (13) (2009) 3876 – 3884.

[26] J. Zhang, Y. Li, Y. Wang, Z. Liu, L. Chen, Y. Chu, F. Zavaliche, R. Ramesh, Effect of substrate-induced strains on the spontaneous polarization of epitaxial bifeo3 thin films, Journal of applied physics 101 (11) (2007) 114105–114105.

[27] S. Shang, Y. Wang, Z.-K. Liu, First-principles elastic constants of α-and θ-al2o3, Applied Physics Letters 90 (10) (2007) 101909.

2

[28] P. Lazar, R. Podloucky, Cleavage fracture of a crystal: Density functional theory calculations based on a model which includes structural relaxations, Physical Review B 78 (10) (2008) 104114.

[29] T. Liao, J. Wang, Y. Zhou, Deformation modes and ideal strengths of ternary layered ti 2 al c and ti 2 al n from first-principles calculations, Physical Review B 73 (21) (2006) 214109.

[30] T. Bučko, J. Hafner, J. G. Ángyán, Geometry optimization of periodic systems using internal coordinates, The Journal of chemical physics 122 (12) (2005) 124508.

[31] K. Momma, F. Izumi, Vesta: a three-dimensional visualization system for electronic and structural analysis, Journal of Applied Crystallography 41 (3) (2008) 653–658.

[32] A. Savin, R. Nesper, S. Wengert, T. F. Fässler, Elf: The electron localization function, Angewandte Chemie International Edition in English 36 (17) (1997) 1808–1832.

[33] R. Hill, The elastic behaviour of a crystalline aggregate, Proceedings of the Physical Society. Section A 65 (5) (1952) 349.

[34] G. Bei, V. Gauthier-Brunet, C. Tromas, S. Dubois, Synthesis, characterization, and intrinsic hardness of layered nanolaminate ti3alc2 and ti3al0. 8sn0. 2c2 solid solution, Journal of the American Ceramic Society 95 (1) (2012) 102–107.

[35] A. A. Voevodin, D. V. Shtansky, E. A. Levashov, J. J. Moore, Nanostructured thin films and nanodispersion strengthened coatings, Vol. 155, Springer Science & Business Media, 2006.

[36] P. Lazar, R. Podloucky, Ab initio study of tension-shear coupling in nial, Physical Review B 75 (2) (2007) 024112.

[37] P. Lazar, R. Podloucky, Ab initio study of the mechanical properties of nial microalloyed by x= cr, mo, ti, ga, Physical Review B 73 (10) (2006) 104114.